

Bioresorbable, Wireless, Passive Sensors as Temporary Implants for Monitoring Regional Body Temperature

Di Lu, Ying Yan, Raudel Avila, Irawati Kandela, Iwona Stepien, Min-Ho Seo, Wubin Bai, Quansan Yang, Chenhang Li, Chad R. Haney, Emily A. Waters, Matthew R. MacEwan, Yonggang Huang, Wilson Z. Ray, and John A. Rogers*

Measurements of regional internal body temperatures can yield important information in the diagnosis of immune response-related anomalies, for precisely managing the effects of hyperthermia and hypothermia therapies and monitoring other transient body processes such as those associated with wound healing. Current approaches rely on permanent implants that require extraction surgeries after the measurements are no longer needed. Emerging classes of bioresorbable sensors eliminate the requirements for extraction, but their use of percutaneous wires for data acquisition leads to risks for infection at the suture site. As an alternative, a battery-free, wireless implantable device is reported here, which is constructed entirely with bioresorbable materials for monitoring regional internal body temperatures over clinically relevant timeframes. Ultimately, these devices disappear completely in the body through natural processes. In vivo demonstrations indicate stable operation as subcutaneous and intracranial implants in rat models for up to 4 days. Potential applications include monitoring of healing cascades associated with surgical wounds, recovery processes following internal injuries, and the progression of thermal therapies for various conditions.

to the core,^[1] as well as from organ to organ,^[2] and even within a given organ.^[3] Accurate evaluations of internal RBTs have strong potential in the context of diagnostic and therapeutic opportunities that cannot be addressed by contact or infrared thermometers for oral, rectal, or epidermal measurements. For example, in the absence of a corresponding increase in core body temperature, a rise in local temperature by 2–4 °C around the site of a surgical process typically indicates the development of an infection.^[4] Temperatures in the intracranial space that increase significantly above normal values (>1 °C) after a traumatic injury correlate strongly to increased rates of mortality.^[5] In the context of regional hyperthermia and hypothermia therapies for certain types of cancer, depression and nerve injuries,^[6] accurate measurements of temperature can guide selection of parameters for optimized outcomes. As most of the medical conditions highlighted

Core body temperature is one of the most essential and commonly used indicators of health status in clinical practice. Because rates of heat dissipation from tissues depend on spatial location, regional body temperatures (RBTs) vary from the dermis

above are temporary, the use of permanent implants as sensing devices^[7]—currently the only means to monitor temperatures inside the body—is nonideal. Prolonged exposure of the surrounding tissues to such sensors increases risks of infection and other

Dr. D. Lu, Dr. M.-H. Seo, Dr. W. Bai, Q. Yang, Prof. J. A. Rogers
Center for Bio-Integrated Electronics
Northwestern University
Evanston, IL 60208, USA
E-mail: jrogers@northwestern.edu

Dr. Y. Yan, Prof. M. R. MacEwan, Prof. W. Z. Ray
Department of Neurological Surgery
Washington University School of Medicine
St Louis, MO 63110, USA


R. Avila, C. Li, Prof. Y. Huang
Department of Materials Science and Engineering
Northwestern University
Evanston, IL 60208, USA

R. Avila, C. Li, Prof. Y. Huang
Departments of Mechanical Engineering and Civil and Environmental
Engineering
Northwestern University
Evanston, IL 60208, USA

Dr. I. Kandela, I. Stepien
Center for Developmental Therapeutics
Northwestern University
Evanston, IL 60208, USA

Dr. I. Kandela, I. Stepien, Prof. C. R. Haney, Dr. E. A. Waters
Chemistry Life Processes Institute
Northwestern University
Evanston, IL 60208, USA

Prof. C. R. Haney, Dr. E. A. Waters
Center for Advanced Molecular Imaging
Northwestern University
Evanston, IL 60208, USA

 The ORCID identification number(s) for the author(s) of this article can be found under <https://doi.org/10.1002/adhm.202000942>

DOI: 10.1002/adhm.202000942

complications, while removal of the devices after they are no longer needed demands a secondary extraction surgery, adding cost, pain and various risks to the patient.^[8,9]

A recently developed design strategy that overcomes such challenges involves construction of temperature sensors using bioresorbable materials.^[10–13] Such bioresorbable devices, as a subset of a broader technology characterized as physically “transient,” function in a stable fashion over a time that matches the medical need, and then dissolve completely in surrounding biofluids to yield benign products through hydrolysis or biochemical decomposition. This process eliminates risks of long-term exposure as well as the need for an extraction surgery. Examples of such types of devices include those for electrical sensing of intracranial pressure and temperature,^[8] of electrophysiological signals for electroencephalographic and electrocardiographic mapping,^[9,14] for electrical stimulation as a form of neuroregenerative therapy,^[15] and for optoelectronic tracking of chemical concentrations and temperature changes.^[16] A primary disadvantage of bioresorbable RBT sensors follows from their requirement for wires to transmit information to external readout systems:^[16] percutaneous wires can serve as niduses of infection,^[17] they are prone to mechanical failure,^[18] and they physically constrain movements of the patient.

Wireless, bioresorbable RBT sensors are attractive in this context. Digital wireless schemes such as those based on near-field communication protocols and Bluetooth standards rely, however, on nonresorbable integrated circuits.^[8] Alternative analog wireless transmission techniques that use amplitude- or frequency-modulated radios require active components. All such schemes demand the use of batteries^[19] or harvesting systems^[8,15,20] for power supply, thereby adding complexity to the system designs and the implantation procedures. As a result, wireless bioresorbable sensors that exploit passive LC-resonance circuits are of interest, where parameters to be sensed induce changes the capacitance C of a responsive element that forms part of the circuit.^[21,22] Such LC-resonance circuits have, however, two intrinsic features that frustrate use for measurements of RBT. 1) Typical bioresorbable temperature sensors rely on temperature-dependent resistances (thermistors) or voltages (thermocouples), with fixed capacitance, while capacitive temperature sensors use nonresorbable materials.^[23] 2) The responses of bioresorbable sensors tend to drift with timescales of minutes to hours to days due to material degradation and/or water permeation, thereby causing difficulties in accurate tracking of parameters, such as temperature, that change over similar timescales. Certain wireless sensors reported in the literature, specifically those that respond to pressure, also have some level of temperature dependence in their operation.^[22] This characteristic could, in principle, form the basis of a temperature sensor. In practice, however, optimizing the response and decoupling the effects of temperature from other parameters are difficult, particularly for applications in RBT sensing.

Here we present materials, fabrication processes, device designs and performance characteristics, along with in vitro and in vivo demonstrations, of a wireless, fully bioresorbable, LC-resonance-based passive temperature sensor with a detection range >2 cm, a precision (random noise level) of <0.05 °C, an accuracy (error compared to a standard thermometer) of ≈ 0.5 °C, and a drift (long-term changes of the result) of ± 0.5 °C un-

der physiological conditions. A key design feature is the use of polyethylene glycol (PEG), a polymer that exhibits a strong temperature dependent dielectric constant near body temperatures (34–42 °C), in a parallel plate capacitor. A layer of natural wax serves as a water barrier encapsulant to suppress drift, for stable operation for up to 6 days in buffer solutions and 4 days when implanted in rat models. Demonstration experiments involve continuous, real-time monitoring of subcutaneous and intracranial temperatures in these animals, with quantitative comparisons to measurements using nonresorbable standards.

The temperature dependence of the dielectric constant (ϵ_r) of PEG arises from the gradual “freezing” of rotational degrees of freedom of the PEG molecules below their melting point. Such freezing decreases the ability of PEG to screen electric fields by rotation of hydroxyl groups along the polymer backbone,^[24] thereby reducing ϵ_r in this temperature range. An analytical expression that phenomenologically describes $\epsilon_r(T)$ is the Curie–Weiss formula^[25] (Figure S1, Supporting Information; theoretical models for the dielectric constant of PEG do not exist, to the best of our knowledge)

$$\epsilon_r = \epsilon_s + (\epsilon_l - \epsilon_s) \frac{T_m - T_C}{T - T_C} \quad (T < T_m) \quad (1)$$

where ϵ_s and ϵ_l are the dielectric constants of the solid phase at low temperature and the liquid phase at the melting temperature, while T_m and T_C are the melting temperature and effective Curie temperature determined by the molecular weight M_w of PEG, respectively. Defining the measurement range from the melting temperature to the temperature when ϵ_r decreases 90%, where the drastic ϵ_r change happens, gives $T_C + 10(T_m - T_C) < T < T_m$. For experiments reported here, $M_w = 1500$, corresponding to $T_m = 47.2$ °C and $T_C = 48.8$ °C (Figure S1, Supporting Information), suitable for measurements across a physiological range (34–42 °C; **Figure 1a**). Note that ϵ_r shows negligible dependence on frequency for the range of interest (10–1000 MHz; Figure S2, Supporting Information). Using PEG as the dielectric in a parallel plate capacitor yields a structure with capacitance, C , that depends strongly on temperature, as a capacitive signal for an LC-resonance-based passive sensor (Figure 1b, inset). The low loss tangent of PEG in this temperature range (<0.1; Figure 1a) leads to negligible leakage currents, which allows high-quality factors $Q \approx 20$, and therefore narrow peaks for precise determination of the resonance frequency. Connecting C to an inductor (inductance L , resistance R) forms an LC circuit (Figure 1b,c) that resonates at a frequency $f_s = 1/2\pi\sqrt{LC} = f_s(T)$. Near-field magnetic coupling of L to a readout coil L_0 enables remote sensing of f_s through measurements of the impedance Z as a function of frequency f across L_0 (Figure 1b,c). A plot of $\text{Re } Z$ versus f manifests as a peak around f_s . Fitting these measurements to the following functional form deduced from the equivalent circuit (Figure 1c) yields the resonance frequency of the sensor^[26]

$$\text{Re } Z = \frac{Kf^2}{1 + Q^2(f/f_s - f_s/f)^2} \quad (2)$$

where other fitting parameters are quality factor $Q = \sqrt{L/C}/R$, and coupling constant $K = 4\pi^2 M^2/R$ (M is the mutual inductance

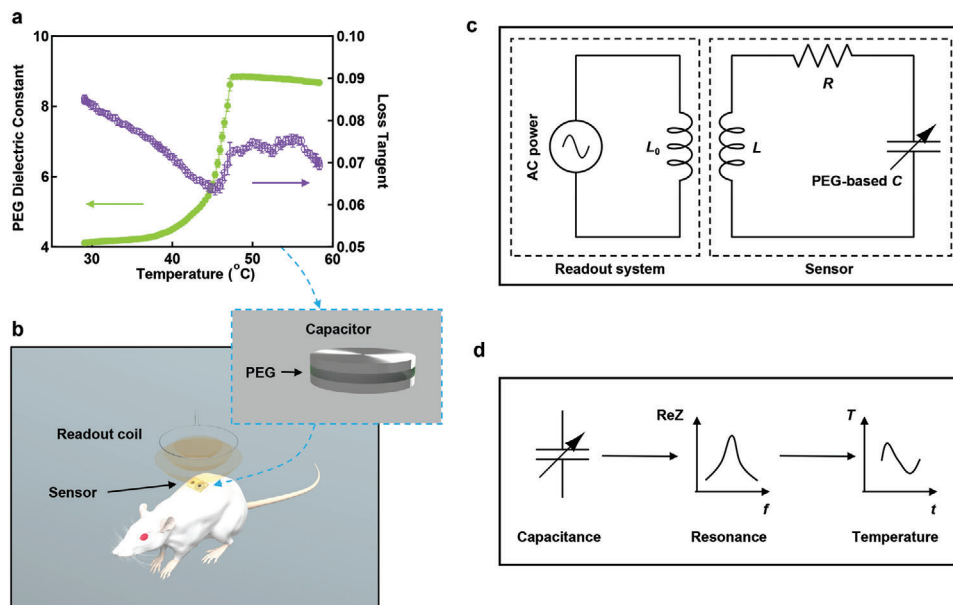


Figure 1. Sensing mechanism for bioresorbable, passive, wireless temperature sensors. a) Dielectric constant and loss tangent of PEG ($M_w = 1500$) as a function of temperature. b) Schematic illustration of wireless sensing based on an implanted LC-resonance-based sensor coupled to an external readout coil; inset, schematic illustration of the structure of a PEG-filled parallel plate capacitor. c) Equivalent circuit of (b). d) Flowchart for the signal conversion process.

between L and L_0). The value of K affects only the amplitude, but not the shape of the resonance, suggesting that determining f_s is robust against the distance and angle between the sensor and the coil. Measuring f_s for a series of known temperatures yields $f_s(T)$, and a conversion from f_s to T (Figure 1d). Continuous monitoring of f_s also naturally yields temporal variations in temperature.

Figure 2a–d schematically illustrates the structure of the sensor and the assembly process. Laser cutting a 100 μm thick magnesium foil yields a six-turn, 1.2 cm diameter coil that connects to the bottom electrode of the capacitor (4 mm diameter). Sandwiching an ≈ 50 μm thick PEG layer between the bottom electrode and a corresponding top electrode (Mg, 100 μm) while using structures of poly-L-lactic acid (PLA, 50 μm) as spacers forms a capacitor (Experimental Section; Figure 2d). Cutting four holes at the end of the coil, and guiding an electrical lead to the top electrode through the holes forms a “twisted” connection. Fixing the connection with conductive wax (tungsten–wax mixture, Experimental Section; Figure 2b,c) mechanically strengthens the joint. Subsequent encapsulation by poly-lactic-co-glycolic acid (PLGA, 10 μm) and a wax-based water barrier layer completes the fabrication (Experimental Section; Figure 2d). The resonance frequency changes with temperature in the expected way. The shape of the curve agrees well with simulated results based on the dielectric constants for PEG (Figure 2e,f). More than 20 fabricated sensors show similar dependence of resonance frequency on temperature, as a validation of the reliability of the design. The calibration function $f_s(T)$ also agrees with simulation, with little temperature hysteresis (Figure 2g). Fitting the calibration function with the Curie–Weiss formula converts f_s to T , and comparing the temperature measured by the wireless sensor to that of a standard technique defines the accuracy of the sensor (0.5 °C; Figure S3, Supporting Information).

An important performance parameter associated with such devices is the operating range. Increasing the vertical distance, or separation z , reduces the signal strength in terms of $\text{Re} Z$ (Figure 3a,b), which also increases noise-induced uncertainties in measurements of temperature (converted from the error of f_s using the calibration function), as characterized by the standard deviation of repetitive measurements (Figure 3c). Defining the detection range as the distance between the sensor and the readout coil when the precision is ± 0.05 °C at 37 °C determines the vertical operating range of the sensor described in Figure 2 (outer diameter OD = 12 mm) as ≈ 1.2 cm (Figure 3c). This operating range applies across a large range of axial angles ($< 30^\circ$, Figure 3d; Figure S4, Supporting Information). Such phenomena can be explained in terms of the magnitude of $\text{Re} Z$, which mainly depends on the mutual inductance M between the sensor and the readout coil, and therefore their relative position. Finite element analysis for their magnetic coupling strongly supports this explanation—the simulated decay of the signal strength with increasing relative distance and axial angle (Figure 3e,f; Figure S5, Supporting Information) closely resembles the experimental data (Figure 3b,d). Simulation also suggests that changing the geometry of the coils, here the diameter as an example, affects the magnetic coupling and therefore strongly influences the operating range of the sensor (Figure 3f). Specifically, increasing OD from 12 to 16 mm (Figure S6, Supporting Information) increases the range from ≈ 1.2 to ≈ 2.2 cm, while decreasing OD to 8 mm yields a miniaturized sensor but with a range of only ≈ 0.6 cm, as also confirmed experimentally (Figure 3d).

Encapsulating the sensor with a material such as natural wax^[27] forms an effective water barrier for stable operation. The weak inflammatory responses of natural wax materials after implantation represent evidence of their biocompatibility.^[28] Two critical parameters control the accuracy of the measurement – the

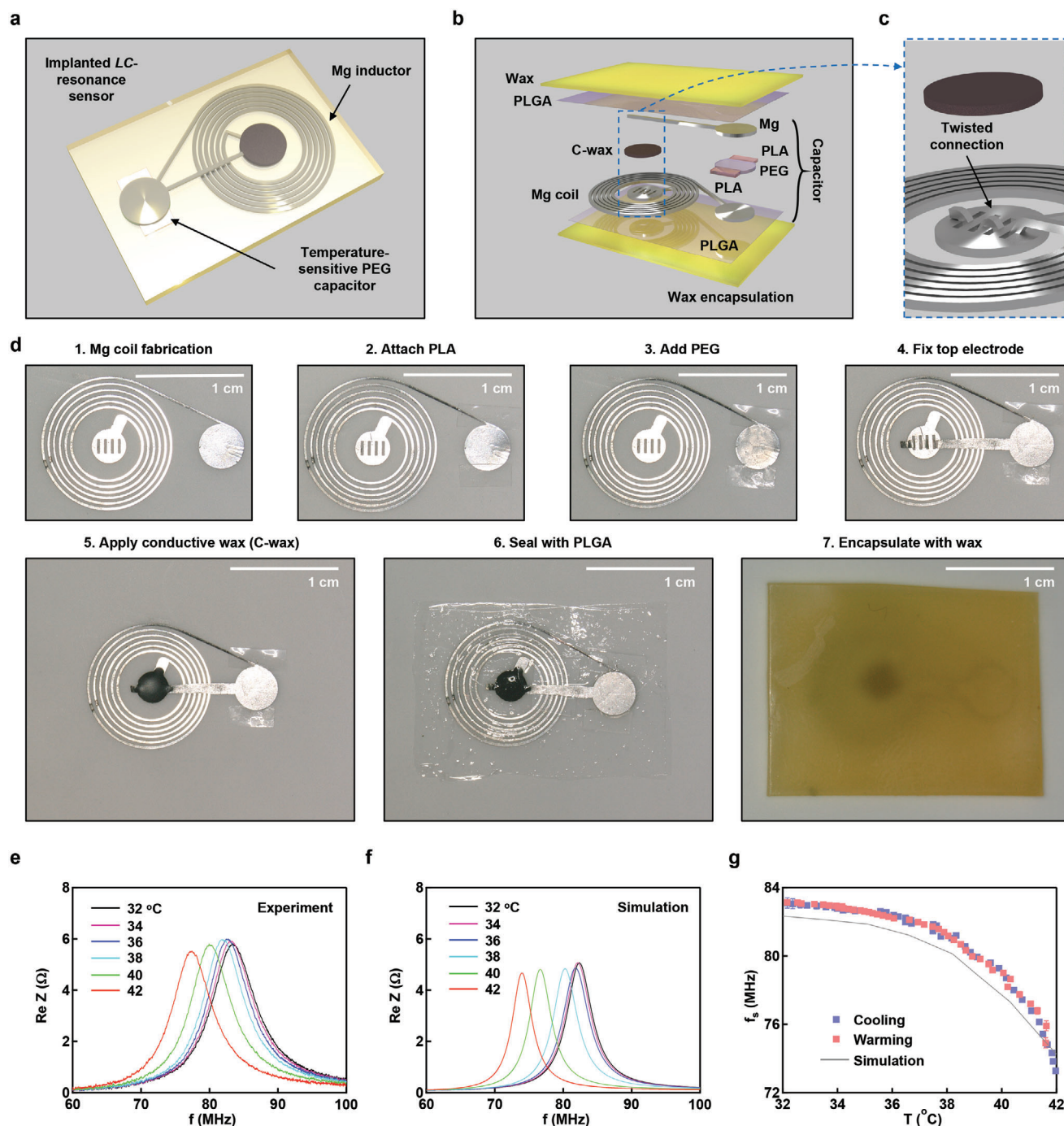


Figure 2. Fabrication and basic characterization of the temperature sensors. a) Schematic illustration of a sensor showing the spiral coil inductor and the PEG-based capacitor. b) Exploded schematic illustration of the structure of the sensor. C-wax, conductive wax. c) Detailed structure of the “twisted” electrical connection between the top electrode and the coil. d) Steps for fabricating a temperature sensor. e) Measured shifts of the LC-resonance peak of a sensor as a function of temperature r . f) Simulation results for the resonance peaks under conditions similar to those of the experiments in frame (e). g) Measured and simulated calibration curves $f_s(T)$.

baseline value of the resonant frequency (f_s at 37 °C) and the sensitivity (df_s/dT at 37 °C). In phosphate buffered saline (PBS, at 37 °C), both the baseline and the sensitivity of sensors coated with 500 μm thick wax are stable from Day 1 to Day 6 (Figure 4a,b): the drift of the baseline and the sensitivity are within ± 0.5 °C,

and $\pm 2\%$, respectively. After Day 6, the baseline drifts down and the sensitivity drifts up, likely due to water permeation. The large dielectric constant of water in this frequency range (≈ 80) may increase the parasitic capacitance of the sensor coil, thereby reducing f_s . Permeation of water into the PEG lowers its melting

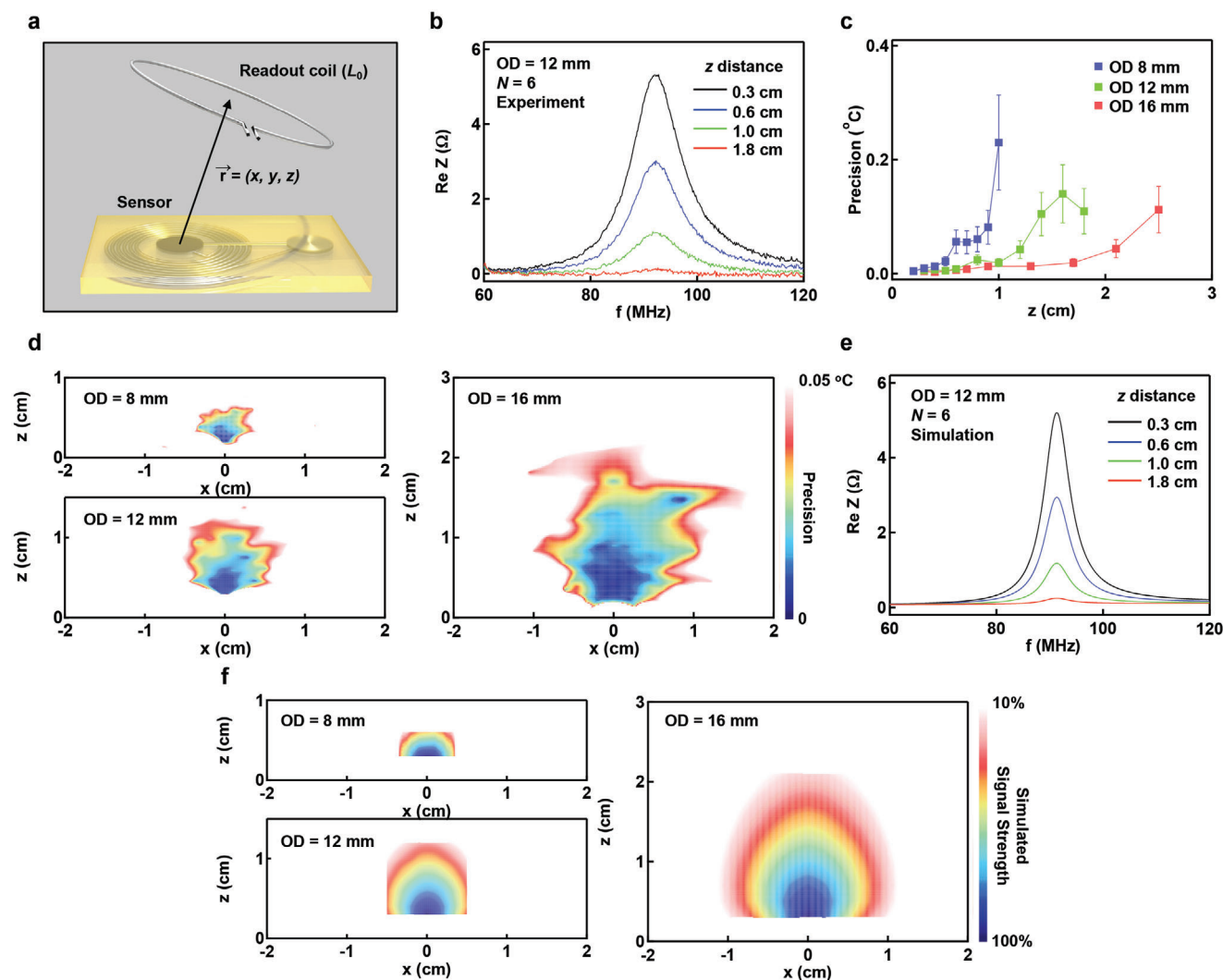


Figure 3. Measurements and simulations for the detection range of the temperature sensors. a) Schematic illustration of the relative position of the sensor and the readout coil. b) Signal strength as a function of distance in the vertical configuration ($x = y = 0$). OD, outer diameter; N , number of turns. c) Simulated signal strength for (b). d) Measurement precision of the temperature as a function of distance in the vertical configuration for sensor coils with different dimensions. e) Measurement precision as a function of vertical distance z and horizontal distance x for sensor coils with different dimensions. f,g) Simulated signal strengths for (d) and (e).

point,^[29] to shift the calibration function to the left and to increase the slope of the $f_s - T$ curve (Figure 2g). Reducing the thickness of the wax (200 μm) reduces the stable operation period to 2 d in 37 $^{\circ}\text{C}$ PBS. Sensors with no wax encapsulation drift significantly within a few minutes in otherwise similar conditions (Figure S7, Supporting Information).

The metals, polymers and natural wax materials used in these sensors are all bioresorbable, as confirmed in previous studies. Magnesium reacts with water to form a soluble hydroxide ($\text{Mg} + 2\text{H}_2\text{O} \rightarrow \text{Mg}(\text{OH})_2 + \text{H}_2$).^[11] Tungsten in the conductive wax oxidizes in water to yield a corresponding soluble acid ($2\text{W} + 2\text{H}_2\text{O} + 3\text{O}_2 \rightarrow 2\text{H}_2\text{WO}_4$).^[11] PLGA and PLA degrade into nutritious compounds—lactic acid and glycolic acid,^[12] while wax is biocompatible and degrades *in vivo*.^[13] PEG is a nontoxic polymer that dissolves readily in aqueous solutions and is excreted through natural processes.^[30] Immersing the sensor in PBS at

37 $^{\circ}\text{C}$ demonstrates the dissolution processes at the device level, where all components except the wax dissolve after 69 d (Figure 4c). Removal of the front side of the wax encapsulation highlights the internal structure. Full degradation of the wax may take months or years, given the slow degradation rate (10 μm per month).^[13] Computational tomography (CT; Figure 4d) with a sensor subcutaneously implanted in the dorsal region reveals the *in vivo* dissolution processes. The clearly visible Mg coil begins to degrade gradually over 2 weeks and eventually disappears on Day 38.

Implanting such sensors in rats allows wireless monitoring of RBT in real time. Figure 5a,b illustrates the implantation of a sensor in a subcutaneous pocket of the dorsal region while the animal is under anesthesia. Wrapping a heating blanket or a water bag at room temperature around the flank of the animal induces changes in body temperature. Measurements with

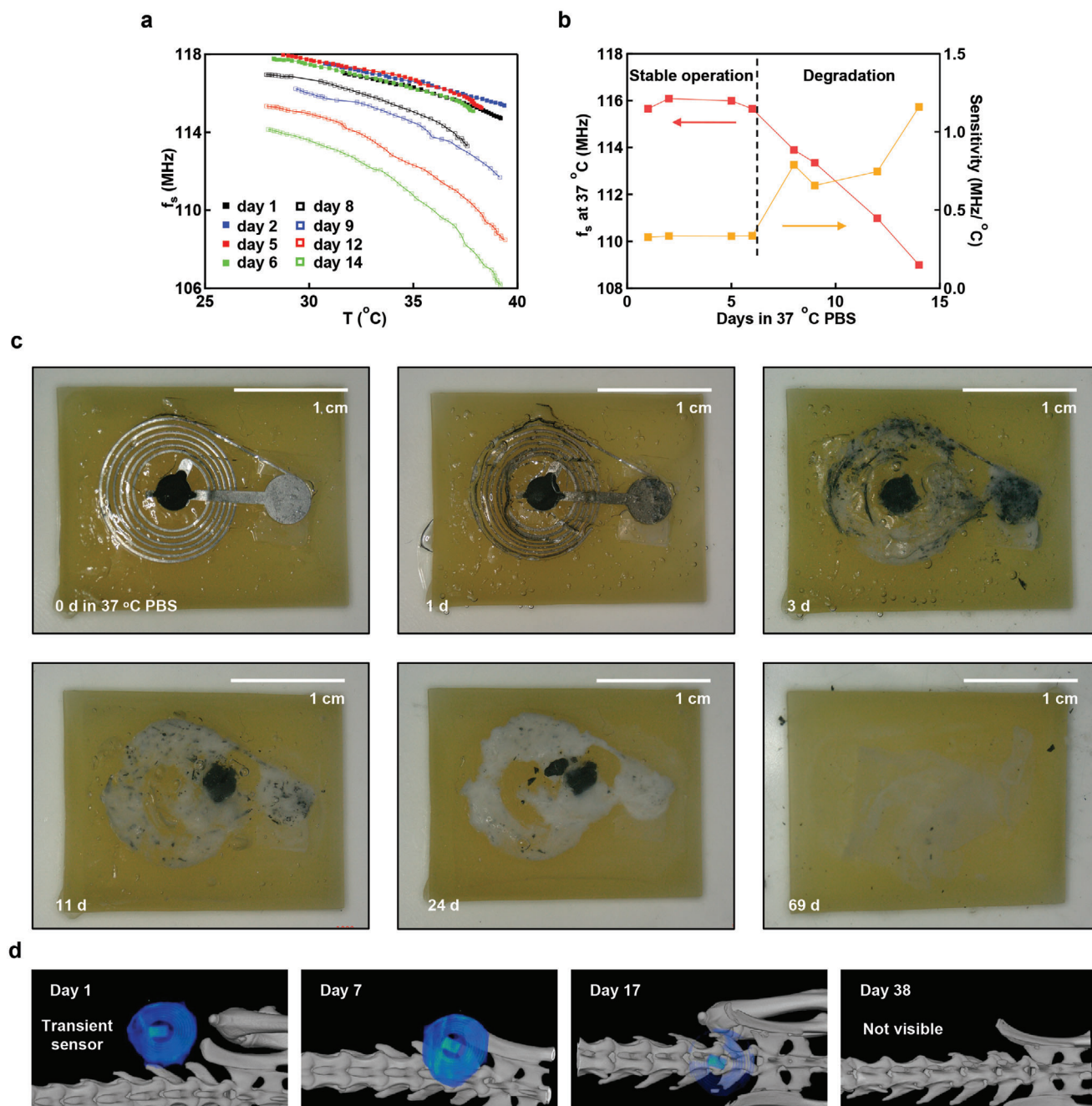


Figure 4. Operational stability and biodegradability of the temperature sensors. a) Drift of the calibration curves $f_s(T)$ in 37 °C PBS. The differences between the resonance frequencies of different sensors arise mainly from differences in the separation between the bottom and top electrodes in the capacitors. b) Drift of the baseline (f_s at 37 °C) and sensitivity (df_s/dT at 37 °C) in 37 °C PBS. c) In vitro biodegradation process in PBS at 37 °C. The front side of the wax encapsulation is removed to show the internal structure. d) Computational tomography of a test structure subcutaneously implanted in the dorsal region demonstrating in vivo biodegradation.

the wireless sensor during these procedures yield data that agree well with those captured using a wired thermocouple inserted into the same subcutaneous pocket under anesthesia (Figure 5c). Figure 5d compares the results of measurements with a thermocouple placed on the skin around the implantation area, an implanted bioresorbable wireless sensor and a rectal probe during warming and cooling processes. At equilibrium, correspond-

ing to the beginning of the experiment, the surface skin temperature is the lowest (≈ 32 °C), the body core temperature is the highest (≈ 36 °C), and the subcutaneous temperature is in between (≈ 34 °C), consistent with expected differences.^[1] Despite its adjacency to the environment, the subcutaneous pocket exhibits temperatures that are robust against changes in the temperature of the surroundings. During changes, the temperature

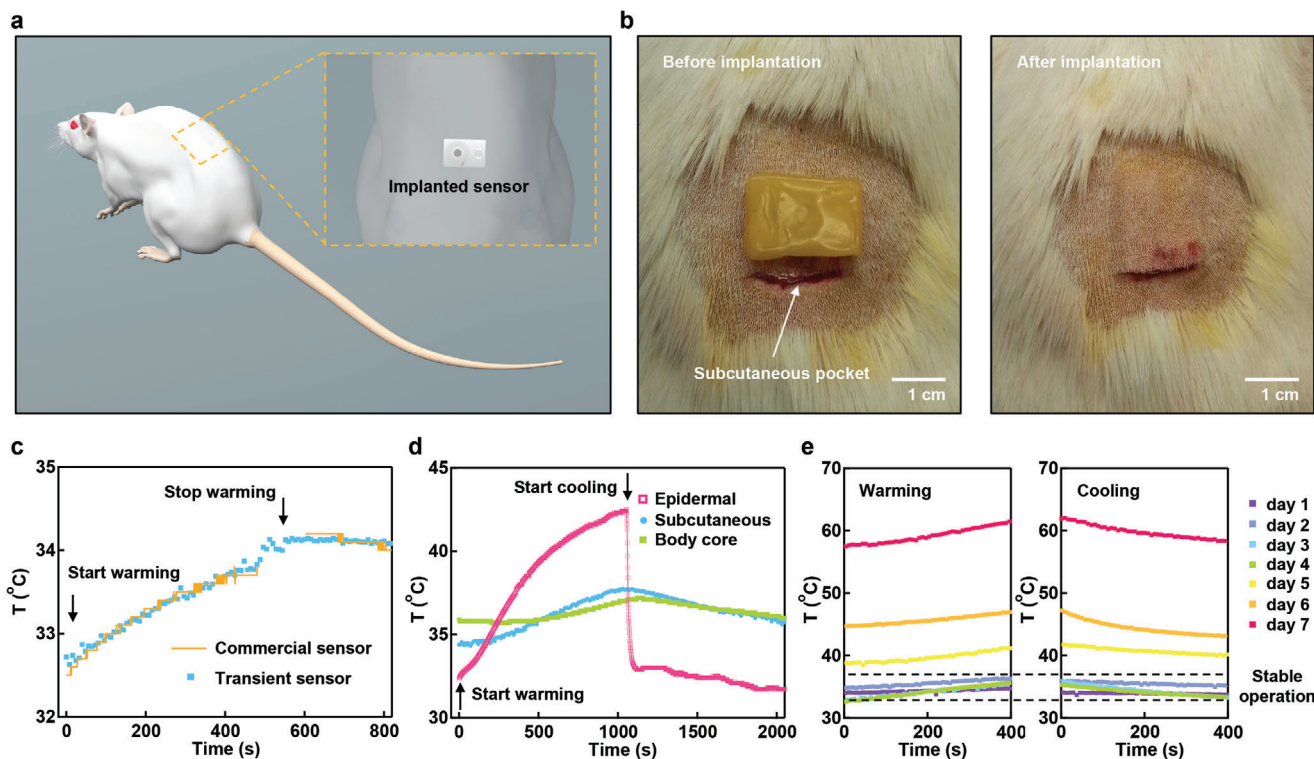


Figure 5. In vivo subcutaneous temperature measurements. a) Schematic illustration of the location of the implanted sensor. b) Procedure for implanting the sensor. c) Subcutaneous temperature measurements using the bioresorbable sensor and a commercial sensor. d) Comparison of the skin temperature, dorsal subcutaneous temperature measured by the bioresorbable sensor and body core temperature in warming and cooling environments. e) Drift of the measured subcutaneous temperature in warming and cooling environments.

of the core lags behind the temperature of the subcutaneous region (Figure 5d). Such phenomena confirm that neither the temperature of the core nor the skin provides a reliable estimation of RBT of the subcutaneous pocket. The temperature captured by the wireless sensor is consistent for the first 4 days following implantation, and then drifts to values of >40 °C (Figure 5e), likely due to material degradation and water permeation as observed through in vitro tests in PBS. The slightly shorter lifetime in vivo may be attributed to the influence of enzymes and other species present in biofluids, or to mechanical effects, that could accelerate the decomposition of the wax encapsulation layer.^[31]

Reductions in the overall size of the sensor are possible through the use of folded designs for the capacitor, with a coil diameter $OD = 8$ mm. The result allows insertion into the limited space between the brain and the inner surface of the skull, where measurements of the temperature of the brain and surrounding cerebrospinal fluid are possible (Figure 6a,b). The experiments involve placing the sensor component of the system in direct contact with the dura mater through a piece of removed skull (≈ 4 mm diameter) and inserting a commercial sensor through a burr hole at an adjacent location (Figure 6c,d). As might be expected, temperatures of the core and the skin are different from those of the brain (Figure 6e). As before, temperature captured from the wireless sensor is consistent for 4 days (Figure 6f). In this case, the change of the core temperature during warming and cooling is larger than that of the brain or the skin, likely be-

cause heating and cooling occurs on the flank, separated from the head (Figure 6e).

These bioresorbable passive sensors allow for accurate, wireless measurements of local temperatures at targeted regions inside the body. A defining feature is that the systems consist entirely of bioresorbable materials, configured to allow stable operation for a clinically relevant period of time, followed ultimately by complete dissolution into benign and nontoxic products that are expelled through natural body processes. Passive LC-resonance-based designs yield simple devices that operate without separate sources of power supply. Although somewhat larger than wireless sensor designs that use concepts in metamaterials,^[23] our LC-resonance system naturally separates the inductor and the temperature-sensitive capacitor. The result allows the use of relatively large inductors for long detection range, compatible with deep tissue implantation, together with small capacitors for localized measurements of temperature. The biodegradable PEG material serves a key role in these devices to convert changes in temperature into changes in capacitance for wireless measurement via the LC circuit, enabled by the temperature-dependent dielectric constant of this material. The wax-based water barrier layers support reliable operation for 4 days in rats, with minimal drifts in baseline or sensitivity. The thickness of the wax layer defines the lifetime of the sensor. Encapsulation with bioresorbable inorganic materials that have low water permeation rates offers the potential to extend the sensor lifetime without increasing the thickness.^[32] Such modifications may also extend the

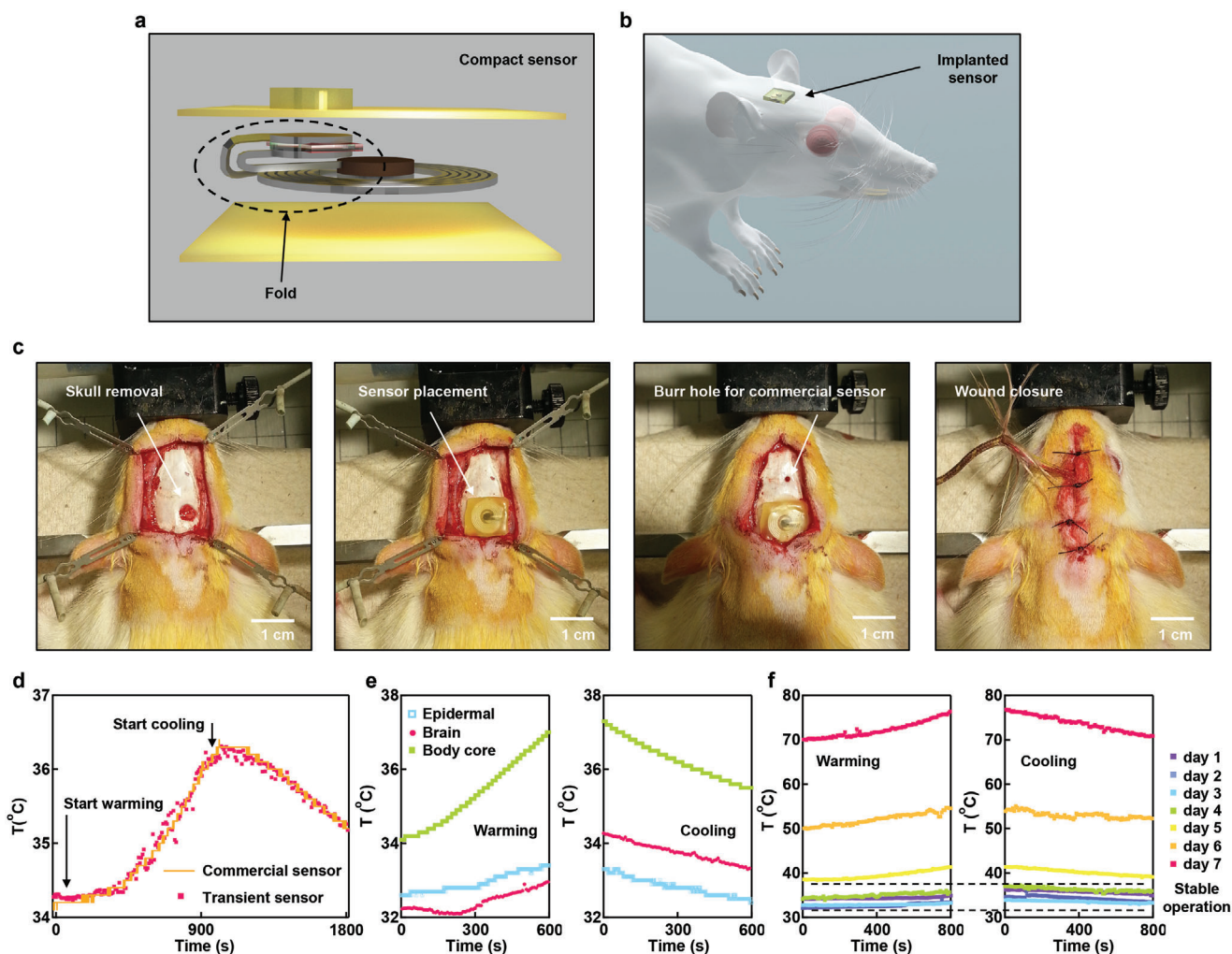


Figure 6. Compact sensors for measurements of temperature in the intracranial space. a) schematic illustration of the structure of the sensor, highlighting the folding of the capacitor. b) Schematic illustration of the implantation location. c) Images that highlight the procedures for implanting the sensor. d) measurements of brain temperature captured with the bioresorbable sensor and a commercial sensor. e) comparison of the skin temperature, brain temperature measured by the bioresorbable sensor and body core temperature in warming and cooling environments. f) drift of the measured brain temperature in warming and cooling environments.

applicability of these sensor from conditions such as acute wound infection to those that involve long term monitoring of temperature.^[33] The sensors do not affect the healing of the wounds for the dorsal subcutaneous pocket; some wounds associated with implants on the head show imperfect healing, likely due to the mechanical stresses applied on the skin due to presence of the implants and the rigidity of the skull.^[34] Reducing the thickness of the encapsulation layer may mitigate such effects. The physical dimensions of the inductor control the detection range, where demonstrated values reach 2.2 cm for inductors with diameters of 16 mm. Use of transmission instead of reflection geometries may provide a route to improving this range without increasing the size of the inductor, to facilitate use in deep tissue regions.^[35] Even in current designs, in vivo measurements of temperature in subcutaneous regions and in the intracranial space demonstrate excellent performance and quantitative agreement with conventional, permanent wired based devices. The results suggest broad applications such as

those in monitoring of infections during recovery from internal wounds, of the status of the brain after traumatic injury, of the temperature during in hyperthermia/hypothermia treatments. Some of the device layouts and materials introduced here may have additional utility in other types of wireless sensors for pressure,^[22] strain,^[35] and electrical potential.^[36]

Experimental Section

Fabrication of the Bioresorbable, Wireless Temperature Sensors: The fabrication began with laser cutting of 100 μm thick Mg foils into spiral coils and top electrodes, followed by immersion in 20 vol% acetic acid for 5 s to remove the surface oxide layers. Etching the leads of the top electrodes in 20 vol% acetic acid for additional 50–60 s reduced their thicknesses to $\approx 10 \mu\text{m}$, to facilitate insertion through the holes formed on the spiral coils. Electrically conductive wax to fix the twisted connection consisted of tungsten powder (C10, buffalo tungsten) and candelilla wax (Sigma-Aldrich) in a weight ratio 15:1.^[13] Techniques based on crimping and other standard

approaches can be considered as alternatives to this type of twisted connection. Heating the sensor to 60 °C allowed application of liquid PEG ($M_w = 1500$, Alfa-Aesar) between the top and bottom electrodes. Adding PLA (50 μm) spacers between the top and bottom electrodes helped to control the thickness of the PEG to $\approx 50 \mu\text{m}$, where applying a small force on the top electrodes facilitated even spreading of the liquid PEG layer between the electrodes. Encapsulation with PLGA (65:35, $M_w = 40\,000\text{--}75\,000$, Sigma-Aldrich) at 70 °C sealed the PEG and prevented interdiffusion between the liquid PEG, conductive wax, and encapsulating wax. Dip-coating the sensor in a molten mixture of beeswax (refined, Sigma-Aldrich) and candelilla wax^[27] at a weight ratio 2:3 at 85 °C yielded a uniform, $\approx 100 \mu\text{m}$ thick encapsulation layer. Multiple cycles of dipping increased the thickness proportionally. Blowing the fabricated sensor with hot air using a heat gun softened the wax to eliminate any local defects in the coating, thereby improving the reproducibility of the sensor lifetime. Each sensor was calibrated individually before use.

Signal Readout and Temperature Measurements: The readout system consisted of a single turn coil (L_0 ; Figure S6, Supporting Information) connected to an Agilent E5062A or an Agilent portable N9923A vector network analyzer. Setting the network analyzer in reflective mode allowed measurement of the real and imaginary parts of the S -matrix element S_{11} . The real part of the impedance across L_0 was then deduced from the following formula

$$\text{Re}Z = Z_0 \frac{1 - (\text{Re}S_{11})^2 - (\text{Im}S_{11})^2}{(1 - \text{Re}S_{11})^2 + (\text{Im}S_{11})^2} \quad (3)$$

where Z_0 is 50 Ω . Sealing the sensors in a plastic chamber (5 cm diameter \times 1 cm height, filled with PBS; Figure S8, Supporting Information) fixed on a programmable hot plate (Torrey Pines HP60) yielded a simple approximate simulation of a physiological environment. An infrared camera (FLIR) monitored the temperature of the sensor. Using a 0.1 °C min^{-1} temperature ramping rate avoided hysteresis-type artifacts in these *in vitro* temperature measurements. Fixing the sensor and the readout coil on a stage implemented with a micrometer and a goniometer allowed measurement of the dependence on distance and angle (Figure 3b–d). Filling the PEG samples in a parallel plate capacitor (1 cm \times 1 cm, 50 μm separation) and connecting to the same vector network analyzer allowed the measurement of the dielectric constant ϵ_r . Specifically, converting S_{11} to $\text{Im}Z$, and then to the capacitance yielded the dielectric constant

$$\text{Im}Z = Z_0 \frac{2\text{Im}S_{11}}{(1 - \text{Re}S_{11})^2 + (\text{Im}S_{11})^2} \quad (4)$$

Finite Element Analysis Simulation: The finite element method was used in electromagnetic simulations to determine the resonance frequency (f_s) change and readout range of the wireless, bioresorbable temperature sensors (OD = 8, 12, and 16 mm; Figure S3, Supporting Information) as a consequence of a change in temperature that increases the matching capacitance in the temperature sensitive PEG capacitor. Each bioresorbable magnesium (Mg) temperature sensor was paired with a single turn copper (Cu) wire readout coil with an OD twice that of the sensor, e.g., a sensor with an OD = 8 mm worked with a readout coil with an OD = 16 mm as shown in Figure S3 (Supporting Information). The simulations were performed using the commercial software ANSYS HFSS (ANSYS), where the lumped port was used to obtain the port impedance Z of the Cu readout coil with a wire diameter of 0.4 mm. An adaptive mesh (tetrahedron elements), together with a spherical surface as the radiation boundary (1000 mm in radius), was adopted to ensure computational accuracy. The dielectric constant (ϵ), electrical conductivity (σ), and dielectric loss tangent (δ) used in the model are $\epsilon_{\text{Mg}} = 1$, $\sigma_{\text{Mg}} = 2.25 \times 10^7 \text{ S m}^{-1}$, $\delta_{\text{Mg}} = 0$ for the magnesium traces; $\epsilon_{\text{Cu}} = 1$, $\sigma_{\text{Cu}} = 5.8 \times 10^7 \text{ S m}^{-1}$, $\delta_{\text{Cu}} = 0$ for the copper wire, $\epsilon_{\text{Wax}} = 2.4$, $\sigma_{\text{Wax}} = 0 \text{ S m}^{-1}$, $\delta_{\text{Wax}} = 0.0093$ for the wax layer; and $\epsilon_{\text{PLGA}} = 4.5$, $\sigma_{\text{PLGA}} = 0 \text{ S m}^{-1}$, $\delta_{\text{PLGA}} = 0.006$ for the PLGA layer. The material properties of the PEG dielectric layer are presented in Figure 1a.

In Vivo Biodegradation Study: All procedures associated with the animal studies followed the recommendations in the Guide for the Care

and Use of Laboratory Animals of the National Institutes of Health. The Institutional Animal Care and Use Committee (IACUC) at Northwestern University approved the protocol (protocol IS00005877). Two female rats (250–350 g, Charles River) were acclimatized up to 5 d before surgery. Animals were anaesthetized using isoflurane gas (2–4%) during the implantation surgery. Presurgical preparation such as hair removal on the surgical area, sterilization of the tools, swabbing the skin surface area with ethanol and povidone-iodine wipes were completed. Creating a subcutaneous pocket at the dorsal region allowed the implantation of a bioresorbable wireless sensor. Coating the Mg coil in the sensor was used here with a 500 nm thick layer of W improved the contrast in CT images, while reducing the amount of applied conductive wax minimized the artifacts due to the scattering of the X-ray from its concentrated tungsten component.^[37] Thinning the wax encapsulation layer to 100 μm also allowed faster degradation of the sensor.

Implantation of Sensors into the Dorsal and Cerebral Locations of Live Animals: All procedures associated with the animal studies followed the recommendations in the Guide for the Care and Use of Laboratory Animals of the National Institutes of Health. The Institutional Animal Care and Use Committee (IACUC) of Washington University in St Louis approved the protocol (protocol no. 20170189). A male Lewis rat weighing 250–350 g (Charles River) received subcutaneous injections of buprenorphine hydrochloride (1.2 mg kg^{-1} ; Reckitt Benckiser Healthcare) for pain management 1 h before the surgical process. The surgical procedures involved anaesthetizing the rat with isoflurane gas inhalation (4% for induction and 2% for maintenance), holding the head in a stereotaxic frame. Following preparation and sterilization of head and dorsal region, a craniectomy on head or a subcutaneous pocket in the dorsal region was made. The bioresorbable sensor was implanted on the skull or in the subcutaneous pocket. For implantation of sensor on the skull, dental cement (Fusio Liquid Dentin) was applied and cured under ultraviolet light to secure the implant on the skull. A commercial thermocouple-based temperature sensor (CT305, Thermco Products) implanted in nearby craniectomy or the same subcutaneous pocket enabled the evaluation of the accuracy of RBTs measured by the wireless sensor. Attaching the thermocouple on the skin and inserting a commercial body temperature sensor (Neulog) into the rectum allowed direct comparison between RBT, temperature of the skin and body core temperature. The wireless readout involved placing the readout coil on top of the head for the intracranial temperature measurement and above the subcutaneous pocket for subcutaneous temperature measurement. The working distance was $\approx 5 \text{ mm}$.

Supporting Information

Supporting Information is available from the Wiley Online Library or from the author.

Acknowledgements

This work utilized Northwestern University Micro/Nano Fabrication Facility (NUFAB) of Northwestern University's NUANCE Center, which received support from Soft and Hybrid Nanotechnology Experimental (SHyNE) Resource (NSF ECCS-1542205), the Materials Research Science and Engineering Center (NSF DMR-1720139) at the Materials Research Center, the International Institute for Nanotechnology (IIN), the Keck Foundation, the State of Illinois through the IIN, Northwestern University, and the Querrey-Simpson Institute for Bioelectronics. The Center for Developmental Therapeutics was supported by Cancer Center Support under Grant No. P30 CA060553 from the National Cancer Institute, awarded to the Robert H. Lurie Comprehensive Cancer Center. R.A. acknowledges support from the National Science Foundation Graduate Research Fellowship (NSF Grant No. 1842165) and Ford Foundation Predoctoral Fellowship.

Conflict of Interest

The authors declare no conflict of interest.

Keywords

biomedical implants, bioresorbable devices, LC-resonance, regional body temperature, wireless sensors

Received: June 3, 2020
Published online: June 29, 2020

- [1] P. Webb, *Eur. J. Appl. Physiol. Occup. Physiol.* **1992**, *64*, 471.
- [2] a) C. Childs, A. Vail, R. Protheroe, A. T. King, P. M. Dark, *Anaesthesia* **2005**, *60*, 759; b) L. McIlvoy, *J. Neurosci. Nurs.* **2004**, *36*, 23.
- [3] K. N. Fountas, E. Z. Kapsalaki, C. H. Feltes, H. F. Smisson, 3rd, K. W. Johnston, J. S. Robinson, Jr., *Neurocrit. Care* **2004**, *1*, 195.
- [4] a) A. Chanmugam, D. Langemo, K. Thomason, J. Haan, E. A. Altenburger, A. Tippett, L. Henderson, T. A. Zortman, *Adv. Skin. Wound Care* **2017**, *30*, 406; b) M. Fierheller, G. Sibbald, *Adv. Skin Wound Care* **2010**, *23*, 369.
- [5] S. Rossi, E. R. Zanier, I. Mauri, A. Columbo, N. Stocchetti, *J. Neurol., Neurosurg. Psychiatry* **2001**, *71*, 448.
- [6] a) M. Andresen, J. T. Gazmuri, A. Marin, T. Regueira, M. Rovegno, *Scand. J. Trauma, Resusc. Emerg. Med.* **2015**, *23*, 42; b) G. Broessner, M. Fischer, G. Schubert, B. Metzler, E. Schmutzhard, *Crit. Care* **2012**, *16*, A1.
- [7] a) A. Koh, S. R. Gutbrod, J. D. Meyers, C. Lu, R. C. Webb, G. Shin, Y. Li, S. K. Kang, Y. Huang, I. R. Efimov, J. A. Rogers, *Adv. Healthcare Mater.* **2016**, *5*, 373; b) B. Silemek, V. Acikel, C. Oto, A. Alipour, Z. G. Aykut, O. Algin, E. Atalar, *Magn. Reson. Med.* **2018**, *79*, 2824.
- [8] S. K. Kang, R. K. Murphy, S. W. Hwang, S. M. Lee, D. V. Harburg, N. A. Krueger, J. Shin, P. Gamble, H. Cheng, S. Yu, Z. Liu, J. G. McCall, M. Stephen, H. Ying, J. Kim, G. Park, R. C. Webb, C. H. Lee, S. Chung, D. S. Wie, A. D. Gujar, B. Vemulapalli, A. H. Kim, K. M. Lee, J. Cheng, Y. Huang, S. H. Lee, P. V. Braun, W. Z. Ray, J. A. Rogers, *Nature* **2016**, *530*, 71.
- [9] K. J. Yu, D. Kuzum, S. W. Hwang, B. H. Kim, H. Juul, N. H. Kim, S. M. Won, K. Chiang, M. Trumpis, A. G. Richardson, H. Cheng, H. Fang, M. Thomson, H. Bink, D. Talos, K. J. Seo, H. N. Lee, S. K. Kang, J. H. Kim, J. Y. Lee, Y. Huang, F. E. Jensen, M. A. Dichter, T. H. Lucas, J. Vimenti, B. Litt, J. A. Rogers, *Nat. Mater.* **2016**, *15*, 782.
- [10] a) S. W. Hwang, G. Park, C. Edwards, E. A. Corbin, S. K. Kang, H. Y. Cheng, J. K. Song, J. H. Kim, S. Yu, J. Ng, J. E. Lee, J. Kim, C. Yee, B. Bhaduri, Y. Su, F. G. Omenetto, Y. G. Huang, R. Bashir, L. Goddard, G. Popescu, K. M. Lee, J. A. Rogers, *ACS Nano* **2014**, *8*, 5843; b) S.-K. Kang, S.-W. Hwang, H. Cheng, S. Yu, B. H. Kim, J.-H. Kim, Y. Huang, J. A. Rogers, *Adv. Funct. Mater.* **2014**, *24*, 4427.
- [11] a) L. Yin, H. Cheng, S. Mao, R. Haasch, Y. Liu, X. Xie, S.-W. Hwang, H. Jain, S.-K. Kang, Y. Su, R. Li, Y. Huang, J. A. Rogers, *Adv. Funct. Mater.* **2014**, *24*, 645; b) H. Tao, S.-W. Hwang, B. Marelli, B. An, J. E. Moreau, M. Yang, M. A. Brenckle, S. Kim, D. L. Kaplan, J. A. Rogers, F. G. Omenetto, *Proc. Natl. Acad. Sci. USA* **2014**, *111*, 17385.
- [12] L. S. Nair, C. T. Laurencin, *Prog. Polym. Sci.* **2007**, *32*, 762.
- [13] S. M. Won, J. Koo, K. E. Crawford, A. D. Mickle, Y. Xue, S. Min, L. A. McIlvried, Y. Yan, S. B. Kim, S. M. Lee, B. H. Kim, H. Jang, M. R. MacEwan, Y. Huang, R. W. Gereau, J. A. Rogers, *Adv. Funct. Mater.* **2018**, *28*, 1801819.
- [14] H. Fang, K. J. Yu, C. Gloschat, Z. Yang, C. H. Chiang, J. Zhao, S. M. Won, S. Xu, M. Trumpis, Y. Zhong, E. Song, S. W. Han, Y. Xue, D. Xu, G. Cauwenberghs, M. Kay, Y. Huang, J. Vimenti, I. R. Efimov, J. A. Rogers, *Nat. Biomed. Eng.* **2017**, *1*, 0038.
- [15] J. Koo, M. R. MacEwan, S. K. Kang, S. M. Won, M. Stephen, P. Gamble, Z. Xie, Y. Yan, Y. Y. Chen, J. Shin, N. Birenbaum, S. Chung, S. B. Kim, J. Khalifeh, D. V. Harburg, K. Bean, M. Paskett, J. Kim, Z. S. Zohny, S. M. Lee, R. Zhang, K. Luo, B. Ji, A. Banks, H. M. Lee, Y. Huang, W. Z. Ray, J. A. Rogers, *Nat. Med.* **2018**, *24*, 1830.
- [16] W. Bai, J. Shin, R. Fu, I. Kandela, D. Lu, X. Ni, Y. Park, Z. Liu, T. Hang, D. Wu, Y. Liu, C. R. Haney, I. Stepien, Q. Yang, J. Zhao, K. R. Nandoliya, H. Zhang, X. Sheng, L. Yin, K. MacRenaris, A. Brikha, F. Aird, M. Pezhouh, J. Hornick, W. Zhou, J. A. Rogers, *Nat. Biomed. Eng.* **2019**, *3*, 644.
- [17] a) M. S. Kim, J. S. Jeong, H. S. Ryu, S. H. Choi, S. J. Chung, *J. Neurol. Sci.* **2017**, *383*, 135; b) M. Rosa, E. Scelzo, M. Locatelli, G. Carrabba, V. Levi, M. Arlotti, S. Barbieri, P. Rampini, A. Priori, *World Neurosurg.* **2017**, *97*, 64.
- [18] A. A. Mohit, A. Samii, J. C. Slimp, M. S. Grady, R. Goodkin, *Parkinsonism Rel. Disord.* **2004**, *10*, 153.
- [19] L. Yin, X. Huang, H. Xu, Y. Zhang, J. Lam, J. Cheng, J. A. Rogers, *Adv. Mater.* **2014**, *26*, 3879.
- [20] a) X. Huang, Y. Liu, S.-W. Hwang, S.-K. Kang, D. Patnaik, J. F. Cortes, J. A. Rogers, *Adv. Mater.* **2014**, *26*, 7371; b) C. H. Lee, H. Kim, D. V. Harburg, G. Park, Y. Ma, T. Pan, J. S. Kim, N. Y. Lee, B. H. Kim, K.-I. Jang, S.-K. Kang, Y. Huang, J. Kim, K.-M. Lee, C. Leal, J. A. Rogers, *NPG Asia Mater.* **2015**, *7*, e227; c) Q. Guo, J. Koo, Z. Xie, R. Avila, X. Yu, X. Ning, H. Zhang, X. Liang, S. B. Kim, Y. Yan, M. R. MacEwan, H. M. Lee, A. Song, Z. Di, Y. Huang, Y. Mei, J. A. Rogers, *Adv. Funct. Mater.* **2019**, *29*, 1905451.
- [21] C. M. Boutry, L. Beker, Y. Kaizawa, C. Vassos, H. Tran, A. C. Hinckley, R. Pfattner, S. Niu, J. Li, J. Claverie, Z. Wang, J. Chang, P. M. Fox, Z. Bao, *Nat. Biomed. Eng.* **2019**, *3*, 47.
- [22] a) M. Luo, A. W. Martinez, C. Song, F. Herrault, M. G. Allen, *J. Microelectromech. Syst.* **2014**, *23*, 4; b) A. Hänninen, T. Salpavaara, J. Lekkala, M. Kellomäki, *Proceedings* **2018**, *2*, 914; c) A. Palmroth, T. Salpavaara, J. Lekkala, M. Kellomäki, *Adv. Mater. Technol.* **2019**, *4*, 1900428.
- [23] a) P. Tseng, B. Napier, L. Garbarini, D. L. Kaplan, F. G. Omenetto, *Adv. Mater.* **2018**, *30*, 1703257; b) H. Karim, D. Delfin, L. A. Chavez, L. Delfin, R. Martinez, J. Avila, C. Rodriguez, R. C. Rumpf, N. Love, Y. Lin, *Adv. Eng. Mater.* **2017**, *19*, 1600741; c) M. Dautta, M. Alshetaiwi, A. Escobar, F. Torres, N. Bernardo, P. Tseng, *Adv. Electron. Mater.* **2020**, *6*, 1901311.
- [24] a) N. E. Hill, *Proc. R. Soc. London, Ser. A* **1957**, *240*, 101; b) J. D. Hoffman, C. P. Smyth, *J. Am. Chem. Soc.* **1949**, *71*, 431; c) N. Koizumi, T. Hanai, *Bull. Inst. Chem. Res., Kyoto Univ.* **1964**, *42*, 115; d) S. Schrodle, R. Buchner, W. Kunz, *J. Phys. Chem. B* **2004**, *108*, 6281.
- [25] G. Rupprecht, R. O. Bell, *Phys. Rev.* **1964**, *135*, A748.
- [26] Q.-A. Huang, L. Dong, L.-F. Wang, *J. Microelectromech. Syst.* **2016**, *25*, 822.
- [27] Q. Yang, S. Lee, Y. Xue, Y. Yan, T.-L. Liu, S.-K. Kang, Y. J. Lee, S. H. Lee, M.-H. Seo, D. Lu, J. Koo, M. R. MacEwan, R. T. Yin, W. Z. Ray, Y. Huang, J. A. Rogers, *Adv. Funct. Mater.* **2020**, *30*, 1910718.
- [28] T. K. Madsboell, R. F. Vestergaard, T. C. Andeliusa, E. M. Haugeband, J. M. Hasenkam, *Eur. J. Cardio-Thoracic Surg.* **2014**, *45*, 476.
- [29] L. Huang, K. Nishinari, *J. Polym. Sci., Part B: Polym. Phys.* **2001**, *39*, 496.
- [30] a) R. Webster, V. Elliott, B. K. Park, D. Walker, M. Hankin, P. Taupin, in *PEGylated Protein Drugs: Basic Science and Clinical Applications* (Ed: Francesco M. Veronese), Birkhäuser, Basel, Switzerland **2009**; b) C. E. Brady, J. A. Divalpa, S. G. Morawski, C. A. Sattaana, J. S. Fordtran, *Gastroenterology* **1986**, *90*, 1914; c) C. B. Shaffer, F. H. Critchfield, J. H. Nair, *J. Am. Pharm. Assoc., Sci. Ed.* **1950**, *39*, 340.

- [31] T. Tsujita, M. Sumiyoshi, H. Okuda, *Lipids* **1999**, *34*, 1159.
- [32] J. Shin, Y. Yan, W. Bai, Y. Xue, P. Gamble, L. Tian, I. Kandela, C. R. Haney, W. Spees, Y. Lee, M. Choi, J. Ko, H. Ryu, J. K. Chang, M. Pezhouh, S. K. Kang, S. M. Won, K. J. Yu, J. Zhao, Y. K. Lee, M. R. MacEwan, S. K. Song, Y. Huang, W. Z. Ray, J. A. Rogers, *Nat. Biomed. Eng.* **2019**, *3*, 37.
- [33] D. Jonkers, T. Elenbaas, P. Terporten, F. Nieman, E. Stobberingh, *Eur. J. Cardio-Thoracic Surg.* **2003**, *23*, 97.
- [34] N. D. Evans, R. O. C. Oreffo, E. Healy, P. J. Thurner, Y. H. Man, *J. Mech. Behav. Biomed. Mater.* **2013**, *28*, 397.
- [35] R. Herbert, S. Mishra, H. R. Lim, H. Yoo, W. H. Yeo, *Adv. Sci.* **2019**, *6*, 1901034.
- [36] S. Y. Liu, X. L. Meng, J. W. Zhang, J. Chae, *Biosens. Bioelectron.* **2019**, *139*, 111336.
- [37] M. Katsura, J. Sato, M. Akahane, A. Kunitatsu, O. Abe, *RadioGraphics* **2018**, *38*, 450.